UNIVERSITY OF SOUTHAMPTON

Faculty of Environmental and Life Science
School of Ocean and Earth Science

A coupled LES and observational approach to improve measurements of ocean turbulence from gliders

by

Jan-Torben Witte
MSc

A thesis for the degree of
Master of Philosophy

March 20, 2022

University of Southampton

Abstract

Faculty of Environmental and Life Science
School of Ocean and Earth Science

A coupled LES and observational approach to improve measurements of ocean turbulence from gliders

by Jan-Torben Witte

Microstructure-equipped autonomous ocean gliders are proving to be an adequate platform for measuring turbulence with the advantage of extended duration and fine resolution measurements. However, it is still unclear how the movement of the glider platform impacts the flow around the attached sensors. The incident along-glider water velocity is not known but essential for the calculation of dissipation rates as errors introduce a significant bias. Steady-state or dynamical flight modules that incorporate all significant forces are required to compute the set of parameters that subsequently can be used for calculating turbulent dissipation rates. In our investigations, we provide more evidence for this method with the help of computational fluid dynamics (CFD) simulations with the large eddy simulation (LES) approach of the flow around the glider and its sensors so that the bias in the velocity flow measurements can be estimated.

Through velocity measurements, velocity shear and therefore turbulent dissipation rates can be determined which are calculated for various ambient dissipation rates ϵ_{am} ranging from $10^{-11}\,\mathrm{m^2 s^{-3}}$ to $10^{-6}\,\mathrm{m^2 s^{-3}}$, thus covering the known range of possible and measurable turbulent motion around the world. This enables our study to investigate the current limits of turbulence measurement on the glider platform and advises caution for the application of glider-based turbulence measurements in low-energetic (i.e. Arctic Ocean) or featureless abyssal plains of the oceans. For high levels of turbulence with the ambient dissipation rate greater than $10^{-9}\,\mathrm{m^2 s^{-3}}$ our results of the flow simulation indicate only small effects of the self-induced strain rate with a ratio less than 1.5 comparing the measured dissipation rate ϵ_{meas} in the simulation with the ambient dissipation rate.

These results attest the glider platforms suitability for turbulence measurements in most areas around the world but also indicate an underestimation of measured flow speeds around the probe tips of the microstructure probe by up to 15%, which should be taken into account for the calculation of turbulent dissipation rates.

Contents

List of Figures

Chapter 1

Introduction

1.1 Motivation

Ocean turbulence is sporadic, chaotic and, therefore, difficult to understand and predict. Yet it is critical to understand and simulate turbulence, and its associated mixing, to predict ocean dynamics and the complex interactions that control the global carbon cycle and the earth's climate.
Without the existence of turbulent mixing, the ocean is stably stratified in density with almost no vertical transport of energy, momentum and important scalars such as heat and nutrients. Energy input from mechanical (wind, tides) and thermal (temperature and salinity changes) processes generates mixing through the breaking of internal waves in the ocean interior and at topographic features at the boundaries as well as through boundary layer processes and provides a steady source of vertical density flux driven by the turbulent energy-cascade in the ocean. Thus, mixing plays a pivotal role in transferring energy to every part of the ocean and inhibits the stratifying effects of the strong density gradient.
We still have a disparity between the parametrization of the turbulent dissipation rate ϵ through field measurements and the level of accuracy that general ocean circulation models require to correctly predict turbulence in the ocean environment. Due to its complexity and range in length scales, a complete and extensive dataset of turbulent dissipation rates is rarely achieved as technologies for fine-scale measurements are just evolving.
The lack of a consistent, dense and extended data set has been always a challenge for every area of oceanographic research and hampers the development of more refined models for the prediction of momentum, heat and salt transfer in the ocean. A comprehensive data set is especially valuable when requiring calibration parameters for a model or when model results have to be validated with experimental results.
Although desirable, it is difficult to achieve a complete data set only with vessel-based instrumentation since the costs of a research vessel are not negligible and the time span

at disposal or the range of measurements are limited (e.g. Palmer et al. (2013); Simpson et al. (1996)). If more complete data sets are necessary, measurements within extended time periods can only be achieved under considerable cost and effort (e.g. Moum et al. (1989); MacKinnon and Gregg (2003a)).
Especially the measurement of ocean turbulence is a crucial part of the comprehensive data set that we are aiming to achieve. Extensive mapping of turbulence and a better understanding of mixing efficiencies potentially provides the key to reveal the drivers and locations of energy dissipation (Munk and Wunsch, 1998).

1.2 Measurement of ocean turbulence

Measuring turbulence in the ocean is challenging even with platforms carefully designed for these purposes. Every sampling of fluid properties will be affected by flow stagnation or separated wakes.
In general, small-scale energy-dissipating velocity fluctuations can be measured by so-called microstructure profilers. These profilers are equipped with an airfoil-shaped shear probe (a few millimeters long), sensing transverse velocity fluctuations caused by turbulent eddies, while the profiler is passing through the fluid (Osborn and Crawford, 1980). The measurements require a stable platform moving unimpeded through the water column to sample temporally and spatially the turbulent fluctuations which lead to the development of different horizontal and vertical profilers (Lueck et al., 2002). The drawbacks of these measuring approaches include, amongst others, the restriction to a research vessel or to a location including the problem of selective sampling (measurement only in mixing hotspots or excluding extreme weather events due to safety reasons (Palmer et al., 2015)).
Another reliable but more autonomous method to measure turbulence is the glider platform which has already been extensively used within the research community at different locations in the ocean to recover the dissipation of kinetic energy ϵ (e.g. Merckelbach et al. (2010); Beaird et al. (2012); Fer et al. (2014); Palmer et al. (2015); St. Laurent and Merrifield (2017); Schultze et al. (2017); Evans et al. (2018); Merckelbach et al. (2019)). Other advantages include an easy deployment, a quick mission adaptability, long endurance and the possibility of sampling the water column horizontally and vertically at the same time, implying a saw-tooth path (Jones et al., 2005).
However, it is still challenging to predict the glider flight completely as its exact location is only known at the surface through two-way satellite communication; the glider velocity, angle of attack and ascent/descent angle is then modelled accordingly. Various modelling approaches for solving this problem have been tested (Jenkins et al., 2003; Graver, 2005; Bhatta, 2006; Williams et al., 2008; Merckelbach et al., 2010; Claus et al., 2012) with the most convincing approach from Merckelbach et al. (2010) expanded in recent years. Assuming steady water and planar flight, an empirical, quasi-static model

for the glider flight was developed to estimate the vertical water velocities and compare them with the measured velocities (Merckelbach et al., 2019).

Using this framework to calculate the horizontal glider velocity, glider measurements of dissipation rates have been conducted successfully in recent years. Since the introduction of microstructure probes on the glider platform several investigations attempted to determine the lower threshold of measuring dissipation rates with the glider platform. Wolk et al. (2009) and Fer et al. (2014) found even for low energy spectra of $\epsilon = 5 \cdot 10^{-11} \mathrm{m^2 s^{-3}}$ an acceptable shape following the Nasmyth's curve (empirical turbulence spectrum measured by Nasmyth (1970) and tabulated by Oakey (1982) which has been accepted by the oceanographic community as being representative of the spectral form of oceanic turbulence (Wolk et al., 2002)) St. Laurent and Merrifield (2017) reports levels of $\epsilon = 8 \cdot 10^{-11} \mathrm{m^2 s^{-3}}$ as the lower threshold and from Schultze et al. (2017) a measuring range of $10^{-5} \mathrm{m^2 s^{-3}} > \epsilon > 10^{-11} \mathrm{m^2 s^{-3}}$ can be inferred. Therefore the scope of this study will investigate the noise level of dissipation rates from the glider platform around a lower threshold of $\epsilon = 10^{-11} \mathrm{m^2 s^{-3}}$ to better understand under which circumstances the measurement of dissipation rates will be realistically achievable.

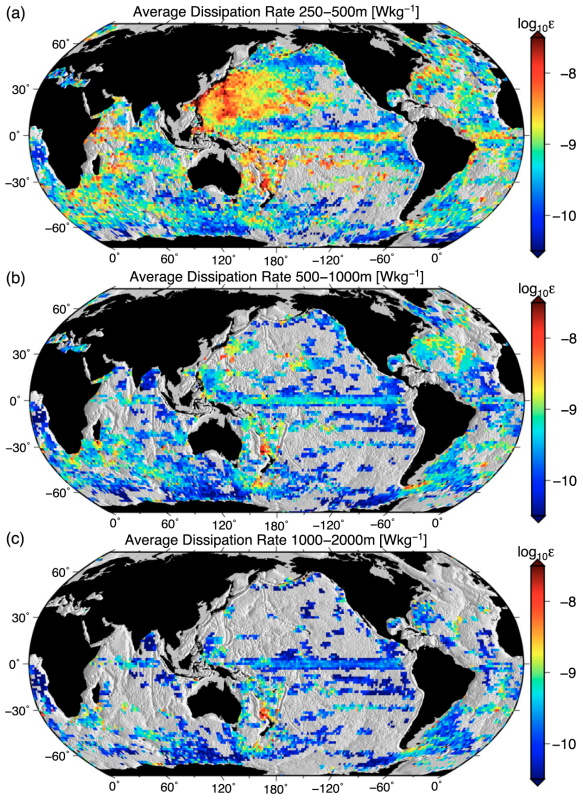

FIGURE 1.1: Average dissipation rate estimates derived by applying strain finestructure methods using Argo profiles between (a) 250 and 500, (b) 500 and 1000, and (c) 1000 and 2000 m. At least three estimates are required to show an average within a 1.58 square bin. These figures are updated from Whalen et al. (2012) and include data from 2006 to 2014. *(taken from Whalen et al. (2015))*

The global distribution of averaged dissipation rates in different depth layers (Whalen et al., 2015, figure 3) indicates that glider-based measurements of dissipation rates will cover the range of the magnitude of turbulence in the upper ocean (> 1000 m) where the majority of dissipation (80-90 %) occurs (Kunze, 2017). Whether the glider is the suitable platform to cover the lower ocean as well due to the low dissipation rates around the noise level is debatable and will be discussed at the end of this study. Nevertheless, the impact of the turbulent dissipation in deep ocean areas is key for the vertical buoyancy flux in the absence of other adiabatic processes (Bardina et al., 1980; Nikurashin and Vallis, 2011) and therefore it is critical to develop suitable methods and platforms to generate turbulence data from this part of the ocean.

1.3 LES simulation for the analysis of glider flight and sensitivity to ambient turbulence

The ability to obtain the correct values for turbulent dissipation rates depends to a large extent on a suitable way to determine the velocities of the glider movement and the surrounding water parcels. Hence, it is of utmost importance to carefully select appropriate values for the flight module parameters and to collect further evidence of the applicability of the flight module.
The correct choice of model approach and critical parameters demands an improved understanding of the hydrodynamic forces around the glider as well as of the impact of the blockage from the geometry on the measured velocities. This can be achieved by simulating the flow around a sensor-equipped glider using computational fluid dynamics (CFD).
Here, different approaches were developed to solve the flow-describing partial differential equations with appropriate initial and boundary conditions. The Reynolds-averaged Navier-Stokes (RANS) equations can be solved for mean quantities using different turbulence models whereas in turbulent-flow simulations like the large eddy simulation (LES) or the direct numerical simulation (DNS), the equations are solved for a time-dependent velocity field (Pope, 2000). These approaches come at different computational expenses as the costs rise from the RANS simulations with fewer and simpler equations to be solved at every time step to the DNS simulations via the LES simulations that calculate the instantaneous fluctuations with far more detail and therefore cosume more computational effort and time. However with the higher accuracy of the LES simulations and especially the DNS simulations, we can directly simulate Reynolds stresses and scalar transport terms that we are deprived of in the RANS simulations through the time-averaging process.
For our purpose, the LES approach offers the best possibility to create a model domain in real-sized dimensions to fit in a glider with resolving the small-scale velocity and force fluctuations around the various sensors at the same time. Especially the ability

to account for the large-scale motions and their substantial contributions and influence on the flow development while increasing computational costs only moderately compared to RANS models, makes LES computations the preferred approach in CFD.
Recent studies of a comprehensive series of wind tunnel experiments with a glider model (Lidtke et al., 2017) and numerical simulations using the LES formulation of the Navier-Stokes equations (Moat et al., 2016) attempt to reveal the effects of the hydrodynamic forces on the glider and try to answer the question whether the measurements of the sensors attached to the microstructure probe are affected by flow distortion around them.
To exploit the possibilities of the improvement in speed, performance and availability of numerical simulations, we chose the model environment of *Basilisk* (Popinet, 2013–2019), a program for the solution of partial differential equations on adaptive Cartesian meshes. The setup of the simulation intended to model the flow around the geometry of a microstructure-equipped glider expands and deepens the results of the simulations that employed *Gerris* (Popinet, 2006–2010), the predecessor of Basilisk (Moat et al., 2016).

1.4 Objectives

There are very few studies (Wolk et al., 2009; Moat et al., 2016) that are trying to link the research done in the vehicle development and simulation of gliders with microstructure dealing with the hydrodynamic properties of the glider and the probe with the research from the oceanographic community that attempts to find novel ways to measure turbulent dissipation more accurately and reliably. As it is evident from the research of the last decades, it is essential to accurately measure the dissipation rates in various places in the ocean to gain a better understanding of the mixing processes. There are several established ways to achieve this (Lueck et al., 2002) but utilising the glider platform appears most promising regarding data sampling density, accessibility and endurance. Here, an open question remains whether the quality of the measured data from sensors, especially the microstructure probe, on gliders is sufficient which was shown in field experiments in numerous studies Merckelbach et al. (2010); Fer et al. (2014); Palmer et al. (2015); St. Laurent and Merrifield (2017); Schultze et al. (2017); Merckelbach et al. (2019). However, confirmation for this approach from numerical studies to understand the flow characteristics around the glider sensors is still missing and needs to be adressed so that the flight characteristics and thus the calculation of dissipation rates from shear measurements can be solidified. With the emergence of more sophisticated tools (Popinet, 2013–2019), we can address the ambiguity surrounding the fluid characteristics around the sensors of a glider and provide a more accurate measurement concept for future studies using the glider platform. Based on the results of Moat et al. (2016) who investigated with a pilot study these fluid characteristics and defined

a model setup for a Slocum glider with an added microstructure probe, our simulations are set up similarly but employ the refined LES code from Popinet (2013–2019).
In this thesis, we employ simulation results for velocities at the microstructure probe tips for a sensitivity study that aims at identifying a threshold up to which turbulence measurements with the current platform design are still reasonable and provide good results. Thus, we will show the suitability of the glider platform for turbulence measurements depending on the turbulent structure of the environment in which the measurements are recorded.
This requires the derivation of a complete set of equations for ocean turbulence in section 2.1 and 2.2 which will enable us in section 2.3 to develop a method testing how the turbulence caused by the shape of the glider influences the measurements of the dissipation rate in different ambient turbulence level scenarios.
We present the approach of the numerical simulation in chapter 3 with the application of the Basilisk code described in section 3.1 and a brief comparison to the results of Moat et al. (2016).
The results of the measurements of the flow field at different positions in the model domain are shown in chapter 4 and are discussed afterwards. The obtained velocity data are used to provide an analysis of shear and dissipation rates to provide an answer for the aforementioned hypothesis.
A conclusion and outlook to possible future follow-up projects is given in chapter 5.

Chapter 2

Theory

The aim of this chapter is to deduce the set of differential equations that govern the processes simulated in the LES approach from the basic principles of fluid mechanics, the conservation of mass, momentum and energy. Following the derivation of Kundu et al. (2012), the equations for these quantities form seven scalar equations with seven unknown variables so that this set of equations can be solved with suitable boundary conditions.

2.1 Derivation of set of equations for turbulence

In this approach, we assume incompressibility ($D\rho/Dt = 0$) and apply the Boussinesq assumption (the negligence of density changes in a fluid except in the gravity force term described by gravitational force g_i) (Kundu et al., 2012) which yields from the conservation of mass the continuity equation

$$\frac{\partial u_i}{\partial x_i} = 0 \quad , \tag{2.1}$$

as well as the set of equations from the conservation of momentum for a Newtonian fluid

$$\frac{\partial u_i}{\partial t} + u_j \frac{\partial u_i}{\partial x_j} = -\frac{1}{\rho_0}\frac{\partial p}{\partial x_i} + \frac{\rho}{\rho_0} g_i + \nu \frac{\partial^2 u_i}{\partial x_j \partial x_j} \quad , \tag{2.2}$$

with the time t, the coordinate directions x_i, the velocities u_i, the pressure p, the density ρ, the reference density ρ_0 and the gravitational force g_i.
The internal energy in the balance of energy for Newtonian fluids obeys a linear relationship to the temperature so that the energy transport equation can be rearranged to a temperature transport equation which simplifies even further for incompressible fluids (Umlauf and Burchard, 2016). Taking into account the reversible heating due to pressure differences at different heights, we will use a slightly different equation

of state and receive a similar transport equation for the potential temperature θ. The temperature transport equations then reads as

$$\frac{\partial \theta}{\partial t} + u_j \frac{\partial \theta}{\partial x_j} - \nu_\theta \frac{\partial^2 \theta}{\partial x_j \partial x_j} = 0 \quad . \tag{2.3}$$

2.2 Reynolds-averaged Navier-Stokes-Equations

For turbulent fluids, the application of the Reynolds decomposition separates the quantities into mean (i.e. $\bar{u}$) and fluctuating, turbulent (i.e. u') parts which yields by inserting this expression into equation 2.1,

$$\frac{\partial u_i}{\partial x_i} = \frac{\partial \bar{u}}{\partial x_i} + \frac{\partial u_i'}{\partial x_i} = 0 \quad . \tag{2.4}$$

When averaged and bearing in mind that the mean of the fluctuations vanishes ($\langle u' \rangle = 0$), we will find the Reynolds-averaged continuity equation

$$\frac{\partial \bar{u}}{\partial x_i} = 0 \quad , \tag{2.5}$$

The same scheme is used for the mean momentum (eq. 2.2) in which the Reynolds decomposition is inserted and averaged to obtain

$$\frac{\partial \bar{u}_i}{\partial t} + \frac{\partial}{\partial x_j}\left(\bar{u}_i \bar{u}_j + \langle u_i' u_j' \rangle - \nu \frac{\partial \bar{u}_i}{\partial x_j}\right) + 2\epsilon_{ijk}\Omega_j \bar{u}_k = -\frac{1}{\rho_0}\frac{\partial p}{\partial x_i} + \frac{g_i}{\rho_0}\bar{\rho} \quad . \tag{2.6}$$

At this point, we have to consider the Coriolis force term arising from the rotation of the earth with the earth rotation vector Ω_j and add centripetal forces to a modified gravity force vector g_i Another new term appearing in this equation different to equation 2.2 is the momentum flux by turbulent motions $\langle u_i' u_j' \rangle$ *(Reynolds stress tensor)*.
The turbulent fluxes can be also found in the temperature transport equation

$$\frac{\partial \bar{\theta}}{\partial t} + \frac{\partial (\bar{u}_i \bar{\theta})}{\partial x_i} + \frac{\partial \langle u_i' \theta' \rangle}{\partial x_i} - \nu_\theta \frac{\partial^2 \bar{\theta}}{\partial x_i^2} = 0 \quad . \tag{2.7}$$

as the turbulent heat flux $\langle u_i' \theta' \rangle$.

2.2.1 Mean and turbulent kinetic energy

The total kinetic energy E is expressed as the sum of mean $\bar{E}$ and turbulent kinetic energy k

$$E = \frac{1}{2}\langle u_i u_i \rangle = \underbrace{\frac{1}{2}\bar{u}_i\bar{u}_i}_{\bar{E}} + \underbrace{\frac{1}{2}\langle u_i' u_i' \rangle}_{k} \quad . \tag{2.8}$$

The kinetic energy of the mean flow evolves from the averaged multiplication of equation 2.6 with $\bar{u}_i$, hence generating the energy equation for the mean flow of a viscous Newtonian Boussinesq-fluid

$$\begin{aligned} \frac{\partial \bar{E}}{\partial t} + \frac{\partial}{\partial x_j}\left(\bar{u}_j\bar{E} + \bar{u}_i\langle u_i' u_j' \rangle - 2\nu\bar{u}_i\bar{S}_{ij} + \frac{\bar{u}_j\bar{p}}{\rho_0}\right) \\ = \langle u_i' u_j' \rangle \bar{S}_{ij} + \frac{g}{\rho_0}\bar{u}_3\bar{\rho} - 2\nu\bar{S}_{ij}\bar{S}_{ij} \end{aligned} \quad . \tag{2.9}$$

The first term is the local rate of change of the mean kinetic energy, the remaining terms on the left hand side of the equation are transport terms for the mean flow, turbulent motion, viscous flow and the flow of pressure and the right hand side displays in the first term the work done against the turbulent Reynolds stress, the second term represents the work against gravity and the last term is the work against the mean stress. The definition of the strain rate tensor $\langle S_{ij} \rangle$ with $\bar{S}_{ij}$ as its mean and S_{ij}' as its turbulent part following Pope (2000) can be written as

$$\langle S_{ij} \rangle = \frac{1}{2}\left\langle \frac{\partial u_i}{\partial x_j} + \frac{\partial u_j}{\partial x_i} \right\rangle \quad . \tag{2.10}$$

The turbulent kinetic energy (TKE) equation can be found through a similar derivation although now we multiply with u_i' before averaging

$$\begin{aligned} \frac{\partial k}{\partial t} + \frac{\partial}{\partial x_j}\left(\bar{u}_j k + \frac{1}{2}\langle u_i' u_i' u_j' \rangle - 2\nu\langle u_i' S_{ij}' \rangle + \frac{\langle u_j' p' \rangle}{\rho_0}\right) \\ = \underbrace{-\langle u_i' u_j' \rangle \bar{S}_{ij}}_{\substack{\text{shear} \\ \text{production}}} + \underbrace{\frac{g}{\rho_0} u_3' \rho'}_{\substack{\text{turbulent} \\ \text{buoyancy} \\ \text{flux}}} - \underbrace{2\nu\langle S_{ij}' S_{ij}' \rangle}_{\substack{\text{rate of} \\ \text{dissipation}}} \end{aligned} \quad . \tag{2.11}$$

The terms on the left hand side of the equation for the local rate of change and the transport of turbulent kinetic energy (TKE) are analogous to equation 2.9. Similarly, the first term on the right hand side describes the work against the Reynolds stress but has the opposite sign indicating that this shear-production term represents the conversion from mean-flow energy to TKE and vice-versa. The turbulent buoyancy flux as the second term can be seen as the conversion between TKE and potential energy. The

last term is the rate of dissipation of TKE (ϵ) into internal energy which takes place if small-scale turbulent motions dissipate due to viscous forces.

2.3 Measurements of turbulence within the simulation

Direct turbulence measurements cannot resolve the Reynolds stress in all spatial directions and therefore only one directional component of the strain rate tensor S_{ij} can be recorded. The measurement technique involving air-foil shear probes follows the concept devised by Osborn (1974). Fixed on a moving underwater vehicle along the x-axis, the probes convert the rate of change of the force into the rate of change of one component of the shear i.e. recording fluctuations dv/dt or dw/dt (Thorpe, 2005). With knowledge of the speed of the platform U, the measurement in time can be rewritten to spatial derivatives $dv/dx = (1/U)dv/dt$ or $dw/dx = (1/U)dw/dt$.
The rate of dissipation of turbulent movements ϵ originates from the last term in eq. 2.11 and therefore reads as

$$\epsilon = 2\nu\langle S'_{ij}S'_{ij}\rangle \quad . \tag{2.12}$$

If we take the definition of the strain rate tensor $\langle S_{ij}\rangle$ from equation 2.10, we can analyse all the diagonal and off-diagonal tensor elements:

$$\langle S_{ij}\rangle = \frac{1}{2}\left\langle \begin{bmatrix} \frac{\partial u}{\partial x} & \frac{\partial u}{\partial y}+\frac{\partial v}{\partial x} & \frac{\partial u}{\partial z}+\frac{\partial w}{\partial x} \\ \frac{\partial v}{\partial x}+\frac{\partial u}{\partial y} & \frac{\partial v}{\partial y} & \frac{\partial v}{\partial z}+\frac{\partial w}{\partial y} \\ \frac{\partial w}{\partial x}+\frac{\partial u}{\partial z} & \frac{\partial w}{\partial y}+\frac{\partial v}{\partial z} & \frac{\partial w}{\partial z} \end{bmatrix} \right\rangle \quad . \tag{2.13}$$

Assuming isotropic turbulence, we can set $u_i = u_j$ and $x_i = x_j$ (Hinze, 1959) so that any spatial derivative of a velocity component normal to it can be used for measurement (Thorpe, 2005; Fer et al., 2014; St. Laurent and Merrifield, 2017; Schultze et al., 2017)

$$\epsilon_{\text{meas}} = \frac{15}{2}\nu\left\langle \left(\frac{dw}{dx}\right)^2 \right\rangle \quad . \tag{2.14}$$

During field measurements, the lower threshold of turbulence detection with the shear probes is influenced by the added turbulence from the geometry of the glider but it is unclear how significant this interference is. With our simulation setup, we can separate the contribution from ambient ϵ_{iw} and glider-caused ϵ_{gl} dissipation rates

$$\epsilon_{\text{meas}} = \epsilon_{\text{am}} + \epsilon_{\text{gl}} \quad . \tag{2.15}$$

As we have total control over the input parameters for the LES simulation, we know that no extra ambient turbulence is included in the setup thus $\epsilon_{\text{am}} = 0$. Therefore, we can obtain values for turbulence measurements ϵ_{meas} that only include the implications of the flow around the glider geometry.

We measure the rate of change of the velocities $(\partial u_i)/(\partial t)$ in all spatial directions in time and thus create an ideal shear probe measurement of the moving vehicle simulated by the initial flow speed of the fluid around the vehicle. This allows us to obtain a value for the dissipation rate in the simulation with the help of eq. 4.1.

2.3.1 Variation of ambient turbulence

Turbulent dissipation in the oceans covers a wide range of length scales and field measurements of the dissipation rates range from $10^{-11}\mathrm{m}^2\mathrm{s}^{-3}$ to $10^{-6}\mathrm{m}^2\mathrm{s}^{-3}$ (see chapter 1.2). For each value of ϵ_{am}, we can calculate the value for the strain rate tensor using eq. 2.12

$$\left\langle \left(S_{ij,\mathrm{am}}\right)^2 \right\rangle = \frac{\epsilon_{\mathrm{am}}}{2\nu} \quad . \tag{2.16}$$

Summing up the two different strain rate tensors $S_{ij,\mathrm{am}}$ and $S_{ij,\mathrm{gl}}$ yields the estimated dissipation rate ϵ_{est} following again eq. 2.12

$$\epsilon_{\mathrm{est}} = 2\nu \left\langle \left(S_{ij,\mathrm{gl}} + S_{ij,\mathrm{am}}\right)^2 \right\rangle \quad . \tag{2.17}$$

This estimated dissipation rate ϵ_{est} describes the influence of the strain that is caused by the geometry of the glider with its attached probes on the ability to measure the dissipation rate while passing through different levels of ambient turbulence.
The ratio of this estimated dissipation rate ϵ_{est} and the ambient dissipation rate ϵ_{am}

$$\epsilon_{\mathrm{rat}} = \frac{\epsilon_{\mathrm{est}}}{\epsilon_{\mathrm{am}}} \quad , \tag{2.18}$$

will help us to determine whether the self-inflicted strain of the glider body alters significantly the accurate measurements of the dissipation rates.

Chapter 3

LES approach

Considering an incompressible fluid for our model simulation, different multigrid solvers for solving the Navier-Stokes equations were developed (Chorin, 1968; Peyret and Taylor, 2012) and extended by higher-order, unconditionally stable advection schemes (Bell et al., 1989). As the flow properties contain a wide variety of scales, adaptive mesh refinement (Berger and Oliger, 1984) which connect classical algorithms on regular Cartesian grids of different resolutions and the refinement through quad or octree discretisations (Khokhlov, 1998) using finite-difference operators for fine or coarse cell boundaries offer a solution to reduce the number of computed cells. This proves to be an important feature of our simulation setup to focus the computational ressources on certain areas of interest or rapidly changing fluid flow with reducing the density of the mesh at places where the flow remains unimpeded from the glider model input.
Popinet (2003) extended the quad/octree implementation of adaptive mesh refinement for incompressible flows and created a numerical method for solving the incompressible Euler equations, combining a quad/octree discretisation, a projection method and a multilevel Poisson solver. This *Gerris Flow Solver* (s. figure 3.1) was extended successively to contain different flow solvers and scenarios (i.e. linearised shallow-water equations (Popinet and Rickard, 2007), multiphase incompressible Navier-Stokes equations (Popinet, 2009)) and transformed to a restructured, high-performance updated framework, called *Basilisk* (Popinet, 2015). This research forms the foundation of the LES simulations that were employed in our study; further details for this code can be found at `http://basilisk.fr/`.

3.1 Experimental setup for model implementation

The most basic principle of the glider technology is the vehicle volume change which causes a change in buoyancy. For increasing the volume against surrounding water pressure, energy needs to be converted into work. This enables the glider to rise

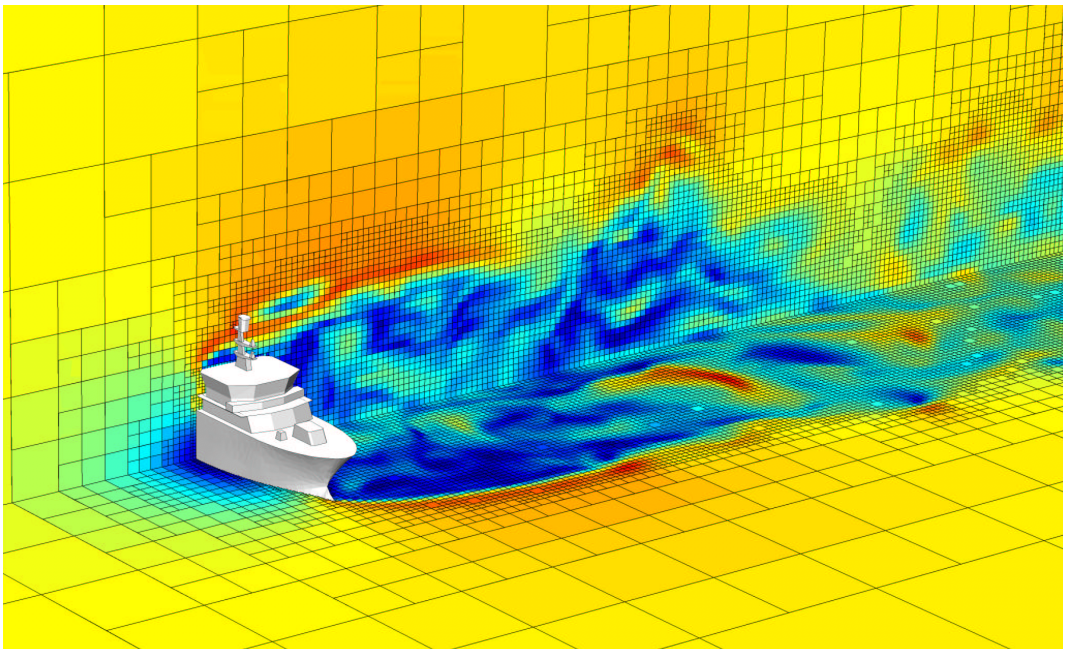

FIGURE 3.1: Air flow around RV Tangaroa with adaptive mesh. The horizontal and vertical cross-sections illustrate the three-dimensional adaptive octree. *(taken from Popinet (2003))*

through the water column while a decrease in volume starts the descent. The glider creates lift and therefore a forward motion when profiling vertically in deviating its axis from the direction of motion, called the angle of attack α. With the steady flight assumption, the centre of buoyancy is located above the centre of mass so that pitch and roll can be controlled by a displacement of the centre of mass (moving the battery packs).
Typically gliders follow paths that are inclined 20° to 30 ° to the horizontal and have an angle of attack of 1° to 3° (Moat et al., 2016). The buoyancy change and the pitch of the vehicle can be chosen by the pilot and influences the speed and the angle of attack according to a steady balance of forces introduced by Merckelbach et al. (2010):

- Weight: downward force depending on mass m of the glider and gravity acceleration g
- Buoyancy: upward force defined by the density ρ, glider volume V and g
- Drag: hydrodynamic force parallel to and opposite to the direction of movement of the glider
- Lift: hydrodynamic force perpendicular to the direction of movement of the glider

Hereby, drag and lift forces are nonlinear functions of the speed and angle of attack.

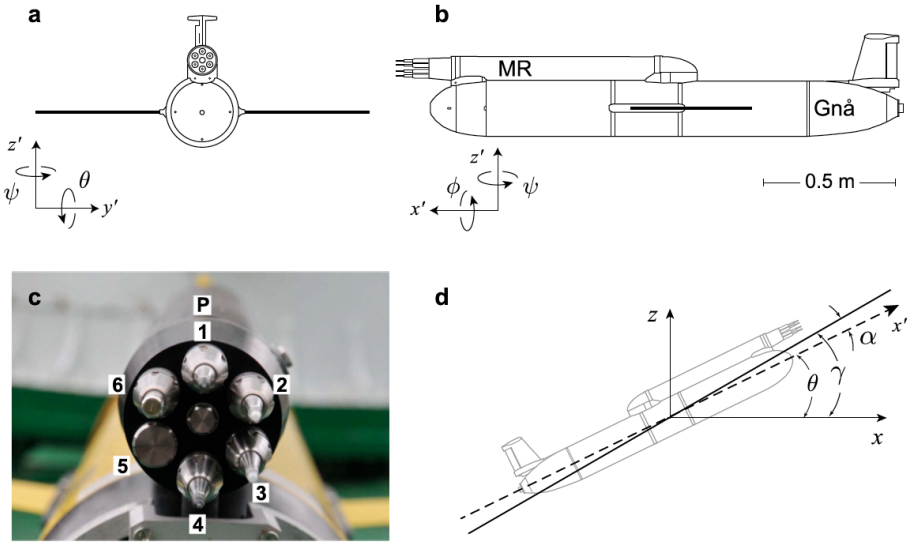

FIGURE 3.2: Schematic diagram of the ocean microstructure glider, OMG. The MicroRider is shown mounted on top of the glider. The front view (a) shows the central location of the microstructure probes relative to the glider body and asymmetry of the combined OMG shape. The side view (b) shows the probe location relative to the front of the glider (tail to the right) and the inclined view (d) depicts all relevant angles required for the calculation of the flight (glide angle γ, pitch θ, angle of attack α). A close-up image of the sensors is shown in (c). *(taken from Fer et al. (Fer et al., 2014))*

3.1.1 Model setup

The flow around the geometry of a glider is modelled with the Basilisk LES code (Popinet, 2013–2019) by solving numerically the time-dependent incompressible Navier-Stokes equations on a non-uniform Cartesian mesh. The code was structured along the example of the air flow around RV Tangaroa from Popinet (2003) that was adapted to the Basilisk platform and can be found at `http://basilisk.fr/src/examples/tangaroa.c` (figure 3.1). Different to the setup in the example, we only consider a one-phase flow but adopt the application of the centered Navier-Stokes solver and the octree discretisation as well as the distance functions for the glider geometry.

The glider geometry model of a Slocum G2 glider with a length of 1.84 m and a diameter of 0.22 m including the Rockland Scientific MicroRider turbulence probe (schematic diagram in figure 3.2) was created from CAD sections by Ben Moat using the open-source CAD program Blender (`https://www.blender.org/`). The final geometry constructed as a single surface with no holes or overlapping parts and repeated vertices includes the turbulence probe and consists of 112,886 vertices (Moat et al., 2016).

The simulation of the flow around the glider is compromising the actual behaviour of the vehicle in its environment. The glider motion is influenced by the density variation of the ambient fluid, the compressibility of the glider body and the vehicle reacts to rudder adjustment or movement of the center of mass. These variations are considered to happen slowly enough compared to the glider moving one body length so that the influence on the calculated parameters is sufficiently negligible if only the glider flight

apart from the turning points is analysed. In the simulation, the input flow is assumed to be uniform and steady with the glider moving at a uniform velocity and constant attitude (ignoring translational and rotational acceleration from hydrodynamics forces). The ambient turbulence ϵ_{am} (section 2.3.1) is not included in the simulation runs but added later artificially to the shear measurements at different locations in the simulation.

3.1.2 Parameter setup

The model domain is formed by a cubic box with a length of $L = 5\,\text{m}$ with closed boudaries except for the inlet at one face of the cube and the outlet at the opposite face thus ensuring a low blockage ratio of the inlet area ($25\,\text{m}^2$) to the glider of 0.6 %. The sufficient domain size was confirmed by probing the flow field in the near-boundary areas which had the same characteristics as the inlet flow field. In the cubic box domain the centre of the glider geometry is placed in the centre of the box while inclining the glider axis with the angle of attack α that is typically rather small (Eriksen et al., 2001) and set to 2.5° (Moat et al., 2016). The glider itself is a full-scale model with a length of $L_g = 1.84\,\text{m}$ and we selected no-slip boundary conitions on its surface. The upstream flow is set to a uniform speed of $U = 0.33\,\text{m/s}$ (average glider velocity, (Palmer et al., 2015)) with the viscosity chosen at $\nu = 1.05 \cdot 10^{-6}\,\text{m}^2/\text{s}$ (sea water at 20° C) so that the Reynolds number yields $\text{Re} = 5.657 \cdot 10^5$. In this way, the water is advected past the glider opposed to an actual glider movement through the water which eventually results in the same simulation characteristics. The properties of the fluid like the seperation of the flow depend on the careful selection of these parameters although testing for the sensitivity of U and ν was outside the scope of this study. To ensure a stochastically steady state flow, the length of the simulation must spin up for the time the flow needs to traverse a distance of several glider lengths. Moat et al. (2016) investigated the time span in which lift and drag had reached equilibrium and equivalent to their study, we assume that the flow reaches equilibrium conditions after 20 s which compares to the flow reaching 3.6 glider lengths downstream bearing in mind the given flow speed U and the glider length L_g.

3.1.3 Simulation specifications

Two different LES simulations were performed for two glider geometry configurations to distinguish effects of the added turbulence probe in the second run while applying the same boundary conditions and flow field parameters.
The minimum cell size of the mesh grid for the turbulent flow field was set to the size of 0.6 mm which equals a resolution level of 13 in the simulation. With the adaptive grid method, the computational grid is updated each time step to sense changes in

the flow field or to enlarge grid cells for areas with a rather steady, uniform flow. The mesh is more refined around the geometry of the glider to resolve the body and the wings as efficient as possible. The total number of grid cells was 16,561,840 without and 19,507,286 with the probe geometry. The 30 s run on 256 (first configuration without the microstructure probe) and 512 (second configuration with the microstructure probe) cores of the 22 TeraFLOP 1152 core HPC cluster at NOC took 230.2 hours (first configuration) and 212.5 hours (second configuration).

Chapter 4

Results from the LES simulation

After intensive refinement of the model setup, the flow simulations using the Basilisk code yielded results for the velocity field and the vorticity for each time step which will be analysed in the following chapter. Additionally, a short review and comparison of the results from Moat et al. (2016) utilising the Gerris flow solver is conducted to establish a benchmark for the novel Basilisk runs.

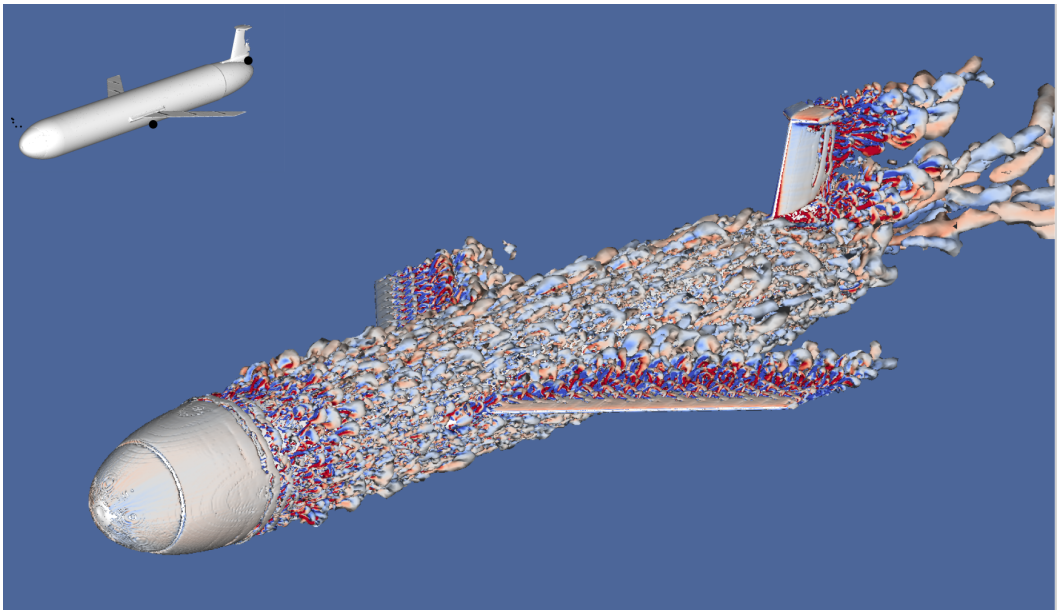

FIGURE 4.1: Vorticity field in the direction of the flow around a glider without the MicroRider on a λ_2 isosurface. The colours indicate positive (red) or negative (blue) vorticity. Small sketch in the upper left hand corner displays the locations of the monitoring points at the sensor positions.

The flow around the glider geometry after 25 s is depicted in figure 4.1 for the configuration without the turbulence package and in figure 4.2 for the setup with the mounted MicroRider. In the top left hand corner of both figures, the position of the

CTD sensor (black dot below the glider body) and the oxygen sensor (black dot behind the glider rudder) and the position of the probe tips (small black dots) are sketched. The λ_2-method which is a vortex core line algorithm identifying vortices from a three-dimensional fluid velocity field (Jeong and Hussain, 1995) can be used to visualise the turbulent eddies that develop through the presence of the glider body.
In figure 4.1, laminar flow can be spotted around the nose of the glider without any recognisable vortices. Further along the glider body, small eddying motions can be discovered although they stay confined to a thin boundary layer around the body and the wings of the glider. A wake is stretching downstream after the flow separates to form larger vortices behind the rudder of the glider. Above the wings the flow is laminar as it is expected in this Reynolds number regime at the beginning accelerates and small wing tip vortices form at the end of the wings.

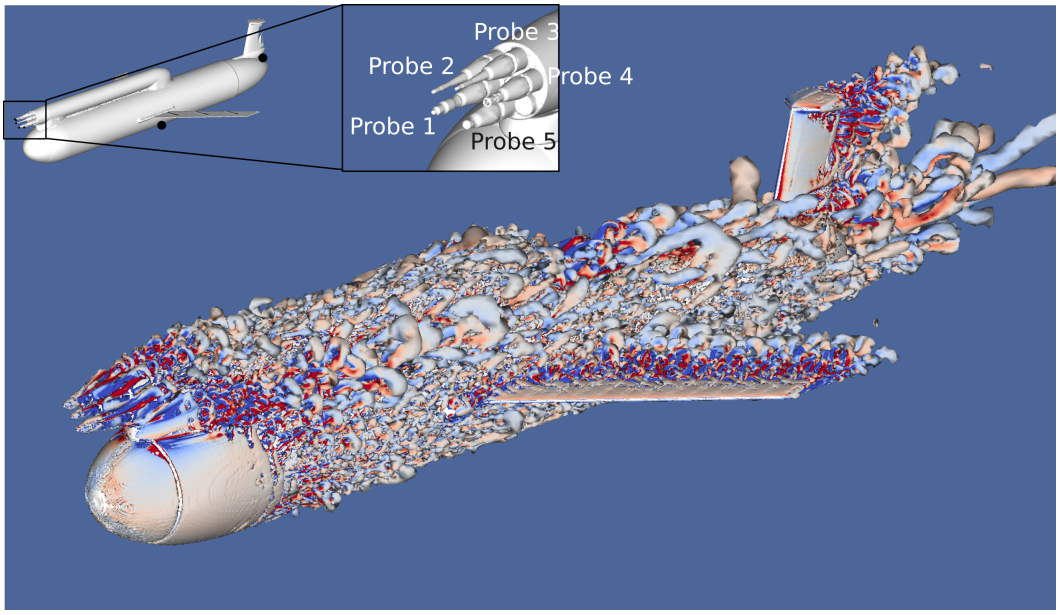

FIGURE 4.2: Vorticity field in the direction of the flow around a glider with the mounted MicroRider on a λ_2 isosurface. The colours indicate positive (red) or negative (blue) vorticity. Small sketch in the upper left hand corner displays the locations of the monitoring points at the sensor positions. Enlarged part shows the shape and position of the probe tips 1-5.

With the addition of the MicroRider on top of the glider body (fig. 4.2), the vorticity on top of the geometry is more enhanced visible by more frequent vortices minima and maxima characterised by intense red and blue colours. This increase in the levels of vorticity originates from adding the MicroRider which adds significant blockage to the otherwise streamlined glider resulting in a thicker turbulent layer with larger vortices on the top of the glider. The flow around the turbulence probe tips seems rather laminar and turbulence-free but the effect of the more pronounced and nearby turbulent eddies could be significant.

4.1 Gerris runs from Moat et al. (2016)

The model runs done with Gerris are described in the study of Moat et al. (2016). The authors find that the u.x-velocity of the flow around the CTD sensor in its position below the body and slightly ahead of the wing base (fig. 4.1, small sketch) is hardly distorted so that the normalised flow (by inlet water speed, 0.33 m/s) in this direction is showing negligible variations (fig. 4.3, left, upper panel, blue) which is no different when the turbulence probe is added (fig. 4.3, left, upper panel, black). On the contrary, the oxygen sensor located on the rear cone (fig. 4.1, small sketch) is affected by the influence of the rudder with a reduced flow of more than half of the free stream velocity or an even stagnant flow (fig. 4.3, right, lower panel, blue). The same observations can be made with the added turbulence probe with an averaged reduction of 50 % of the free flow speed around the oxygen sensor (fig. 4.3, left, lower panel, black) although the flow rate seems to be slightly increased as turbulence is enhanced in this region (Moat et al., 2016). The monitoring points at the probe tips are numbered in

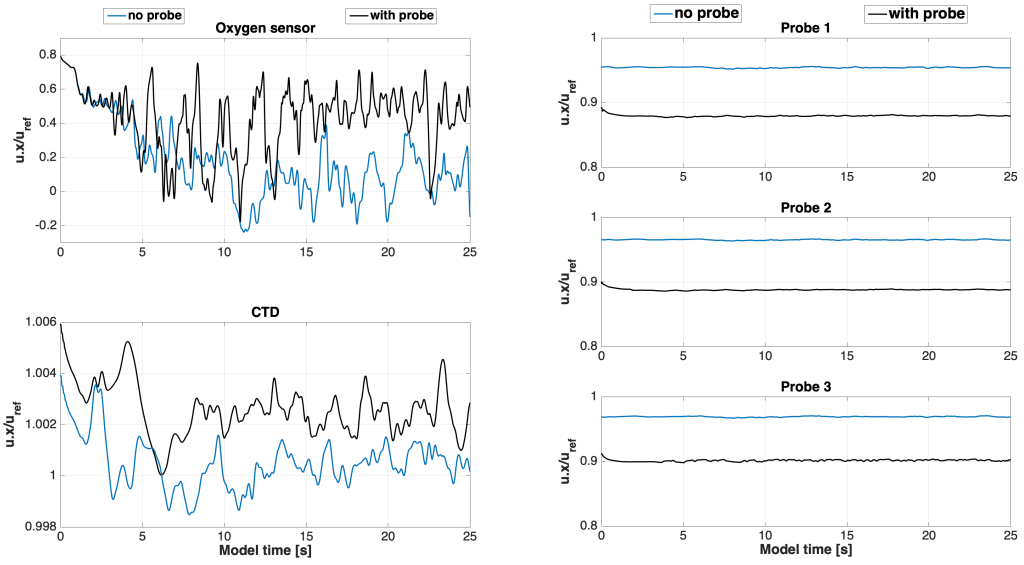

FIGURE 4.3: Results from Gerris runs with different glider geometry configuration (without the probe in blue, with the added probe in black), redrawn from data provided by Moat et al. (2016). Left panels show the along-stream (u.x) flow around the oxygen sensor and the CTD sensor. Right panels show the flow velocities around the probe tips of the microstructure probe.

the same way as in the Basilisk runs (fig. 4.1, enlarged area) and are reported to be sufficiently independent from the mesh resolution (Moat et al., 2016). The results from the study of Moat et al. (2016) are redrawn in figure 4.3 and compared for the two different configurations without (blue) und with the turbulence package (black). Again, the u.x-velocity component is normalised by the inlet water speed of 0.33 m/s. The report finds that the u.x component of the velocity is reduced; 3-6 % without the probe and up to 10 % with the added MicroRider (Moat et al., 2016).

4.2 Basilisk runs

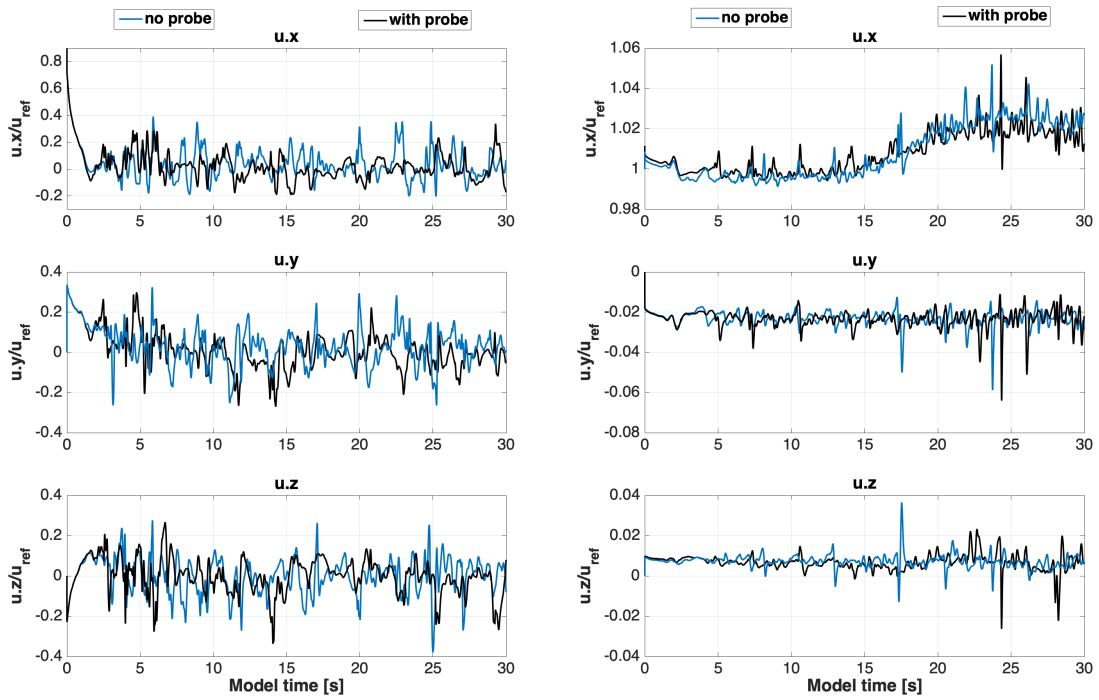

FIGURE 4.4: Results from Basilisk runs with different glider geometry configuration (without the probe in blue, with the added probe in black). Left panels show the along-stream (u.x), cross-stream (u.y) and vertical (u.z) flow around the oxygen sensor. Right panels show the along-stream (u.x), cross-stream (u.y) and vertical (u.z) flow around the CTD sensor.

The simulation runs with the Basilisk code reveal further details on the flow around the sensors (fig. 4.4) and the probe tips (fig. 4.5) in which all velocities are once again normalised by the inlet water speed, 0.33 m/s. The simulation is extended in comparison to the Gerris runs with an additional 5 s to investigate possible underlying oscillations and their impact on the model outcome (Moat et al., 2016). The velocities in u.x-direction (fig. 4.5, left panels) measured at the monitoring points at the probe tips are decelerated by approximately 15 % if the probe is added to the glider geometry. Compared to the reduction without the MicroRider (3-5 %) the altered velocity presumably impacts the measurement at these locations severely which will result in an underestimation of turbulence levels. This can be explained by the enhanced turbulence on the top and at the rear of the glider which may feedback to the probe tips and influence the otherwise quiescent flow at these locations by larger eddying motion. At sensor position 4 and 5, sensors have not been attached to the microstructure probe and are left blank without any further investigations in this report except for the comparison between Gerris and Basilisk code (chapter 4.3).

The observations for the across-stream velocity u.y agree with the results from Moat et al. (2016) with decreasing velocities of less than 1 % from the free inlet stream for the configuration without the probe (fig. 4.5, middle panels, blue) and slightly larger

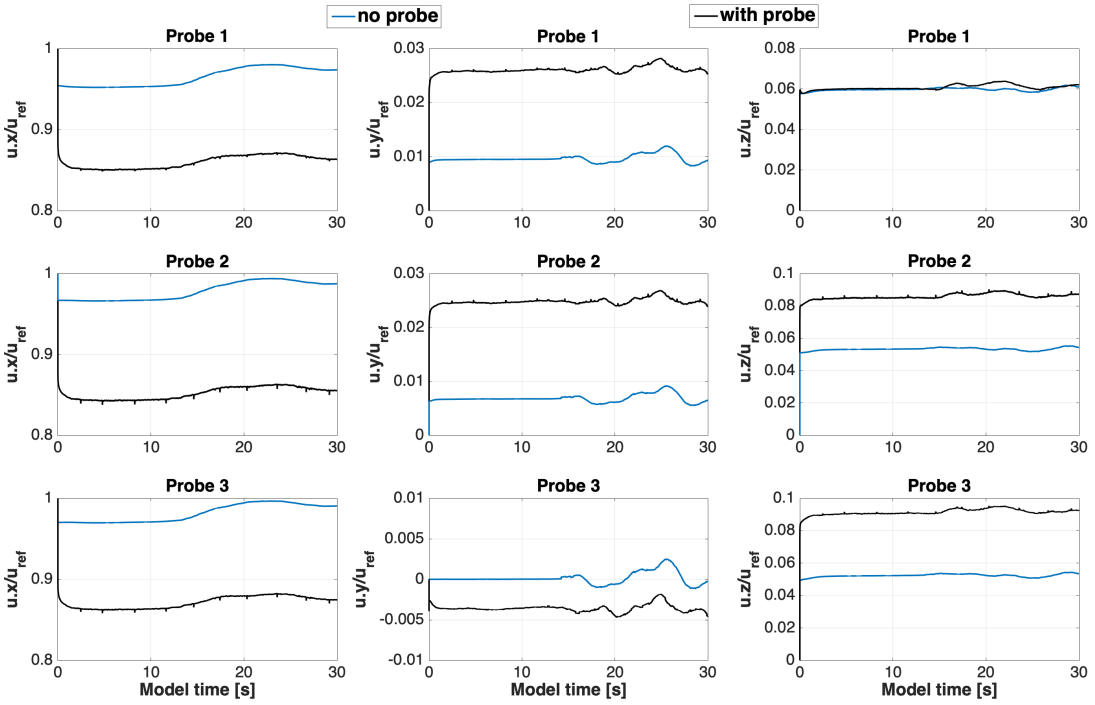

FIGURE 4.5: Results from Basilisk runs with different glider geometry configuration (without the probe in blue, with the added probe in black). Left panels show the along-stream (u.x) velocities, middle panels display the cross-stream (u.y) velocities and right panels show the vertical (u.z) velocities around each probe tip.

values for the velocity deceleration when the turbulence package is added. Here, the variations in u.y from probe 1 and probe 2 deviate from the free stream zero velocity with 2-3 % in the positive direction while the u.y-velocity at the probe tip at location 3 is hardly affected at all. This distribution is due to the flow impinging on the glider geometry and therefore slowing down the across-stream flow in both direction depending on which side of the axis the probes are located on whereas the probe tip in the middle and the furthest away from the glider body just experiences a slight reduction in the u.y-velocity as these effects cancel out.

The reduction of the vertical velocity u.z amounts to 5-10 % of the inlet water speed when the geometry of the glider is used without the MicroRider and is slightly growing towards the position of probe 3 (fig. 4.5, right panels, blue). Except for the position of probe 1, the values will be larger (up to 10 %) when adding the probe to the geometry which seems to be a result of larger turbulent eddies reflected from the glider and the probe body to this region. However, in the near-probe region at position 1, the addition of the probe does not appear to impact the vertical velocities compared the previous configuration.

Interestingly, a gradual increase in velocities is observed around 15 s of the model runs which is then slightly reduced at approximately 27 s so that the deviation appears to change with time in a sine wave pattern. it is not known if this oscillation is due to an error in the LES code or a variation in the pressure field on the surface of the glider. It

is left for further investigations to identify the cause for this demanding longer runs for clarification although this phenomena adds only minor variations to the simulation.

4.2.1 Oxygen and CTD sensors

The oxygen sensor experiences a distinct influence through the rudder presence leading to a largely stagnant flow around the sensor position. This is true for the two different configuration of the glider although the configuration with the added MicroRider seems to cause even larger fluctuations on the flow especially in the across-stream (u.y) and vertical (u.z) directions which vary in the mean by approximately 10 %.
These fluctuations in u.y- and u.z-direction are less pronounced at the position of the CTD sensor with a variation of about 1 to 2 %. Undeniably, it can be stated that the flow field around the CTD sensor consists of smaller turbulent vortices inducing only small variations of the flow whereas the oxygen sensor due to its position in the wake of both the MicroRider and the rudder experiences larger eddying motions. Therefore it is only coherent that the along-stream velocity of the CTD sensors (fig. 4.4, top right hand panel) does not differ massively from the free-stream velocity with a deviation of 1 to 3 % with enhanced velocity levels after the spin-up of the model.

4.3 Comparison of Gerris and Basilisk

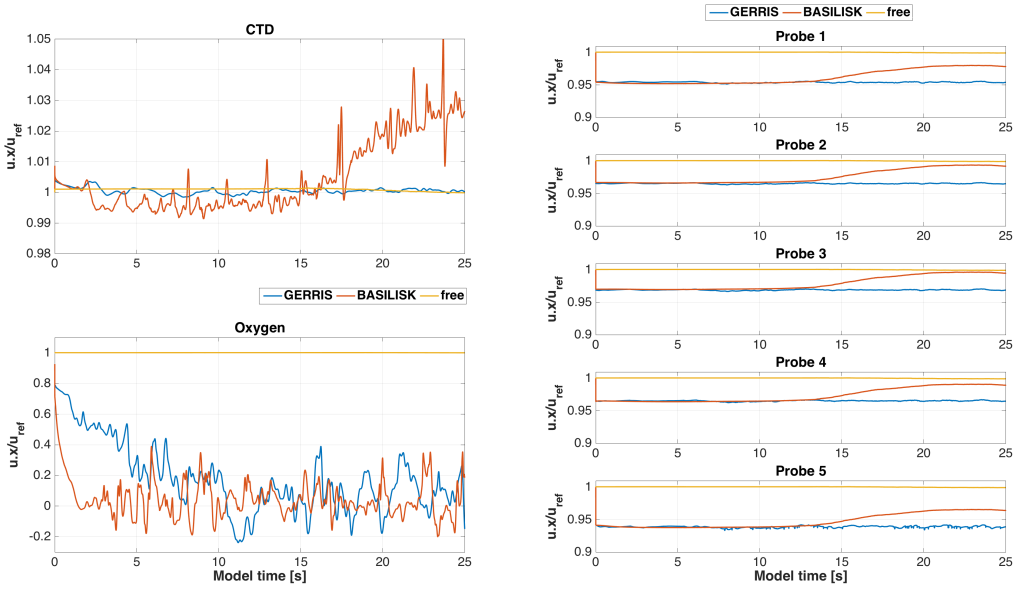

FIGURE 4.6: Comparison of the model runs in Gerris (blue) and Basilisk (red) for the CTD and oxygen sensors (left panels) and the five different probe tips (right panels) without the probe geometry. A reference free-stream value from the Basilisk simulation is displayed in yellow.

The comparison of the different LES codes Gerris and Basilisk offers some understanding of the advantages and disadvantages of both approaches. Figure 4.6 shows a comparison of the along-stream velocities around the sensors and probe tips for both geometry configurations. A reference value of the free stream velocity (the velocity at the same x-coordinate but far away from the glider body and the boundaries of the domain) from the Basilisk simulation is included to underline the differences.
As mentioned earlier, the agreement is fairly good with the only difference in the smoother fluctuations in the Gerris code, especially for the velocities around the CTD sensor. For the flow around the oxygen sensor, the Gerris simulation seems to underestimate the blockage of the rudder and in the second configuration the blockage of the rudder and the microstructure probe combined since the Basilisk code provides a higher accuracy and resolution of the turbulent eddies and therefore identifies more turbulent region that decelerate the flow.
For the flow around the probe, the differences are far less obvious as the results show a good agreement of the Gerris and Basilisk simulation with some smaller deviations for when the MicroRider is added and the velocities around the probe tips of the sensors 2, 3 and 5 are estimated to be slightly reduced in the Basilisk simulation. The only exception is the flow around the tip of sensor 4 with reduced velocities in the Gerris simulation compared to Basilisk.
The aforementioned underlying oscillation in the Basilisk simulation from 15 s onwards which occurs especially in the configuration without the probe in the flow field measurements around the CTD sensor and the probe tips but can also be distinguished in the depiction of the flow around the CTD sensor in figure 4.6 can be attributed to the improved accuracy of the new Basilisk code. The higher resolution and more computed cells and a structurally different code could explain the increase in variability of the velocities measured especially around the CTD sensor in both configurations.

4.4 Discussion of the variation of ambient turbulence

The simulation of the flow field records the instantaneous velocities just in front of the probe tips that we already used to determine the velocity reduction through the addition of the microstructure probe (see section 4.4.2). From this data we are able to calculate velocity shear that develops around the probe tips within the course of the simulation. As explained in section 2.2.3, we can transform our velocity measurements in time to spatial derivatives of the velocity and therefore obtain velocity shear in every direction of our coordinate system.
In our scenario, the glider body is fixed and the water moves with a constant velocity past the geometry, simulating the glider flight in the ocean. Thorpe (2005) describes this situation as a possible mechanism to measure spatial gradients as it is valid to assume a 'frozen' turbulence field according to the *Taylor hypothesis* (Taylor, 1938a,b): During the

time the turbulent field is advected past the probe tip, the measured parameter itself does not change significantly so that the measurement of the temporal variations can be converted into spatial gradients.
As the predominant direction of our velocity fluctuations is the velocity in along-glider direction ($u.x$), we can derive the measured dissipation rate ϵ_{est} with equation 4.1:

$$\epsilon_{\text{meas}} = \frac{15}{2}\nu \left\langle \left(\frac{d(u.x)}{dx} \right)^2 \right\rangle \tag{4.1}$$

Opposed to field measurements in the ocean during which only one spatial direction is measured thus requiring the application of equation 4.1, we can determine the velocity fluctuations in each direction at every times step. By choosing the direction of greatest variability, we select the measurement that introduces the highest amount of glider-induced turbulence to our measurements of the total turbulence, thus causing maximum contamination for the ambient turbulence. With this in mind, we can justify the use of equation 4.1 for the calculation of the measured dissipation rates.

4.4.1 Measured velocity shear and dissipation rate

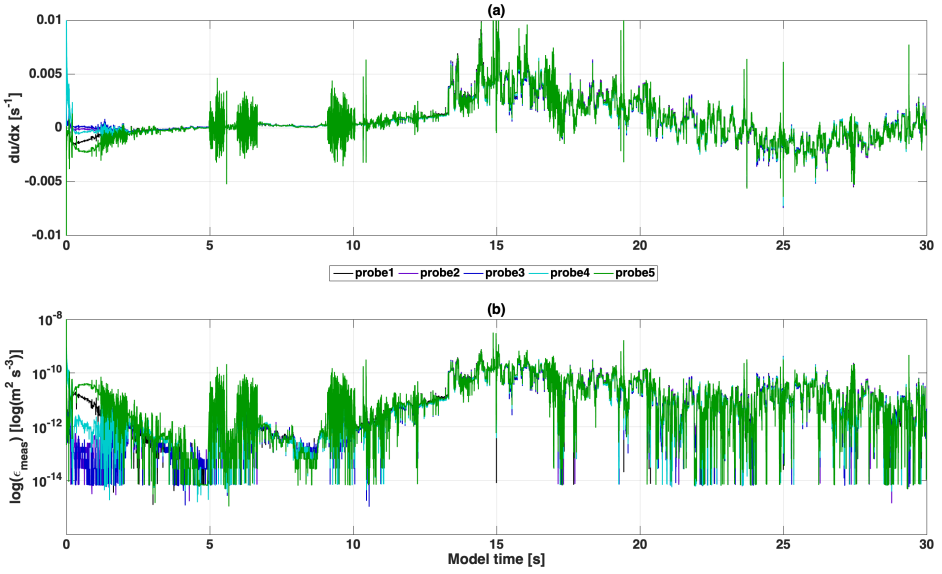

FIGURE 4.7: Measured velocity shear averaged in time for positions of probe 1 to probe 5 (upper panel). Logarithmic dissipation rates ϵ for positions of probe 1 to probe 5 (lower panel).

The velocity shear $d(u.x)/dx$ and the measured dissipation rate ϵ_{est} is displayed in figure 4.7 for all three probes.
It is evident, that the shear (figure 4.7a) at the different positions only slightly differs except for the first seconds when the run-up of the simulation causes non-physical behaviour of the measured parameter. That is evident in figure 4.8, where the data for

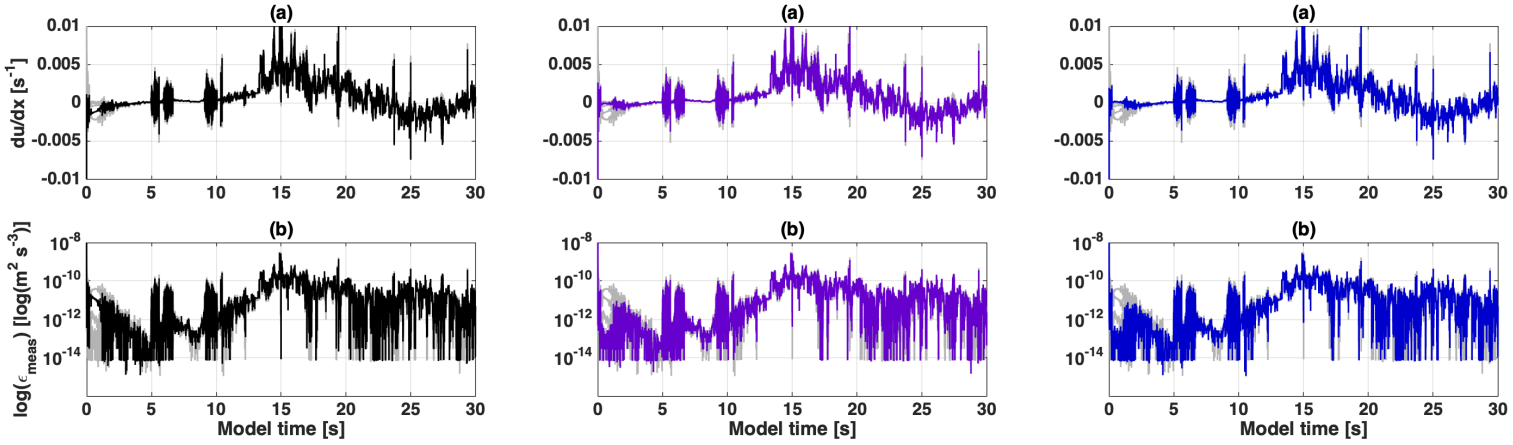

FIGURE 4.8: Measured velocity shear averaged in time and logarithmic dissipation rates ϵ(upper/lower panels). The evolution in time for velocity measurements at the probe tip 1 is displayed in the graphs on the left hand side, the middle panels show probe 2 and the panels on the right hand side show probe 3.

each probe position is displayed next to each other. To flatten out spikes in the velocity fluctuations that translate to the velocity shear, the shear data has been filtered using a simple moving average in time over 0.1 seconds.
After 20 seconds, we can assume to have reached a stochastically steady state (see chapter 3.1.2) and observe a fluctuating shear with a maximum of almost $0.01\,s^{-1}$ which is larger and positive within the period from 15 to 20 seconds and slightly less pronounced and negative in the period of 23 to 27 seconds. This assumption only holds if the underlying oscillation described in chapter 4.2 and 4.3 is not an artefact from the simulation code and needs to re-evaluated in future studies.
The levels of turbulent dissipation presented in the lower panels (figure 4.7b, 4.8b) rise gradually from 10 seconds onwards to almost $10^{-8}\,m^2s^{-3}$ before gradually decreasing to levels around $10^{-11}\,m^2s^{-3}$ to $10^{-10}\,m^2s^{-3}$ showing more variations as the simulation evolves.
Following the introduction of (artificial) additional ambient turbulent dissipation in our calculation ranging from $10^{-11}\,m^2s^{-3}$ to $10^{-6}\,m^2s^{-3}$, the value for ϵ_{est} is calculated for every ϵ_{am} value in that range by making use of equation 2.17. The inherent strain rate of the glider $S_{ij,\text{gl}}$ is found by averaging the strain rate over 2 seconds from 19 to 21 seconds of the simulation when the spin-up is completed and is therefore kept constant. This interval is chosen around 20 seconds when the simulation becomes stable (s. above) with a sufficient large range to filter out the noise in the strain rate.
This finally yields an expression for ϵ_{est} dependent on the added ambient dissipation ϵ_{am} which is displayed as the ratio $\epsilon_{\text{est}}/\epsilon_{\text{am}}$ in figure 4.9.

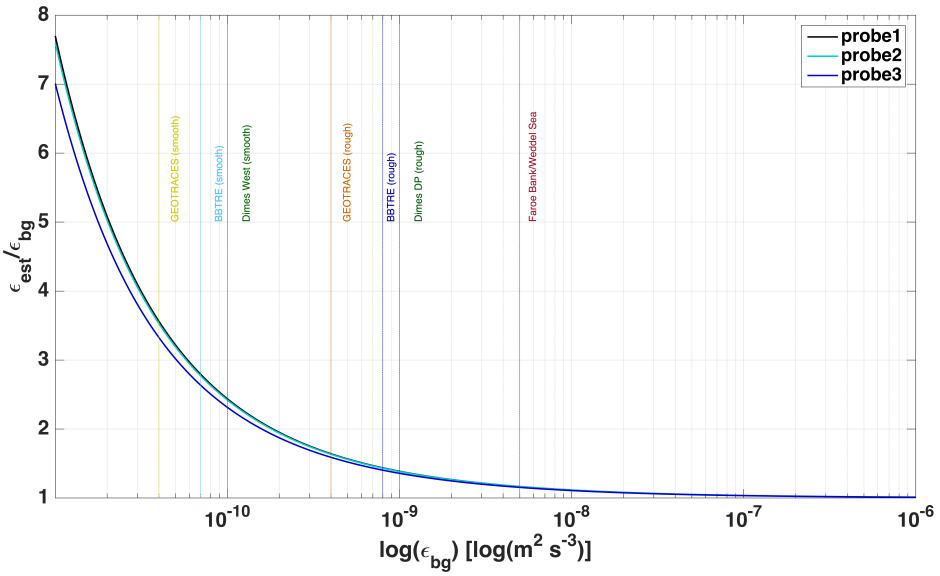

FIGURE 4.9: Comparison of different turbulence levels ϵ_{am} with the estimated turbulence levels ϵ_{est}. Indicated by the coloured dashed lines are the median of various ocean turbulence regimes taken from Waterhouse et al. (2014).

The graph shows a similar behaviour for all three locations and indicates an inverse

relationship between ϵ_{rat} and ϵ_{am}. Looking at low ambient dissipation rates, it is evident that in this regime, the influence of ϵ_{est} compared to ϵ_{am} is far more pronounced and dominates the ratio ϵ_{rat}. Therefore, we can conclude that in areas of low ambient dissipation rates the self-inflicted shear strain of the glider influences the measured dissipation rates ϵ_{est} significantly, hence inhibits the correct measurement of the surrounding turbulence field by the glider.

In turbulent regimes that range from $10^{-11}\,m^2s^{-3}$ to $10^{-9}\,m^2s^{-3}$, the coefficient ϵ_{rat} is larger than 1.5 and therefore does not advocate the use of the glider platform for detecting small-scale turbulence which occurs mainly in the deep basins of the world oceans (Waterhouse et al., 2014). Especially the studies of Ledwell et al. (2000), Polzin et al. (1997) and St. Laurent and Garrett (2002) during the BBTRE project 1996 in the deep Brazil basin in the South Atlantic as well as the measurements of Ledwell et al. (2011) and St. Laurent et al. (2012) in the Antarctic Circumpolar Current west of Cape Hoorn in the Southern Pacific Basin during the DIMES expedition and the data from GEOTRACES in the Western Brazil Basin (Waterhouse et al., 2014) show that the measured dissipation rates are below this critical threshold for a glider in these quiescent water masses if the data are acquired in areas with smooth topography. Similar to those areas, data from microstructure measurements in the Arctic abyssal plains suggests that turbulence is mostly weak (Rainville and Winsor, 2008) and in average often does not exceed levels of $5 \cdot 10^{-10}\,m^2s^{-3}$ to $10^{-9}\,m^2s^{-3}$ (Rippeth et al., 2015).

With the exception of the abyssal plains and the highly stratified low-energetic Arctic ocean, all other areas in the oceans are either shallower or far more diverse in the topography with rougher features or oceanic ridges. Here, higher dissipation rates are observed and attributed to various types of turbulence phenomena. Investigating the impact of lee waves to the turbulent kinetic energy dissipation, Cusack et al. (2017) reports values of $10^{-7}\,m^2s^{-3}$ or even $10^{-6}\,m^2s^{-3}$ impacting the vertical flux of energy that is underrepresented in idealised numerical simulations. Global circulation models are heavily dependent on the correct estimation of mixing efficiency within the hotspots to return dense waters to upper layers of the ocean like the Southern Ocean. A key role is attributed to boundary mixing or mixing over rough topography that is distributed into the ocean interior as reported by Garabato et al. (2019) who observes values around $10^{-9}\,m^2s^{-3}$ to $10^{-7}\,m^2s^{-3}$.

This aligns well with the general study of Waterhouse et al. (2014) where studies in areas with rough topography or close to oceanic ridges dissipation rates are rarely smaller than $10^{-9}\,m^2s^{-3}$ and is exemplary shown in figure 4.9 by the data of the hydraulic overflow at the Faroe Bank Channel (Fer et al., 2010).

Our results show that for the enhanced turbulence greater than $10^{-9}\,m^2s^{-3}$ the ratio ϵ_{rat} converges to 1 as the shear caused by the glider geometry does not hamper the ability to measure the dissipation rates accurately.

Chapter 5

Conclusion and future research

In this study, we can confirm the feasibility of gliders as a platform for the measurement of dissipation rates throughout different turbulent scales especially for areas with dissipation rates in the environment greater than $10^{-9}\,m^2s^{-3}$.
The results from the LES simulation present a comprehensive picture of the flow around a Slocum glider geometry with the added MicroRider so that the position of the equipped sensors and the angle of attack can be critically re-evaluated (section 4.2). The layout of the probe tips for two shear sensors and one fast temperature sensor was evaluated with the key findings that the blockage of the glider body influences the unimpeded flow around the probes with a maximum deceleration of approximately 15 %. This agrees largely with the results from (Moat et al., 2016).
The analysis of the shear recordings in the simulation is utilised to test the sensitivity of the shear probes to artificially introduced turbulence ranging from $10^{-11}\,m^2s^{-3}$ to $10^{-6}\,m^2s^{-3}$ (section 4.4). Here, the added strain from the glider body only influences measurements unduly for low-turbulent environment, hence underlining the suitability of glider-based microstructure measurement for most areas around the world (Whalen et al., 2012; Waterhouse et al., 2014; Whalen et al., 2015; Kunze, 2017).
Caution is needed when operating the glider platform for turbulence measurements in low energetic water masses as the calculation of ϵ from shear measurements in particular can cause a bias towards the noise floor of $10^{-11}\,m^2s^{-3}$ of the sensors (Scheifele et al., 2018). We suggest that measurements in areas with an average ambient dissipation rates smaller than $10^{-9}\,m^2s^{-3}$ are interpreted taking into account the rapid growth of ϵ_{rat} which implies that robust calculation of the measured dissipation rates is potentially impaired.
However, the setup of the simulation is done in an idealised environment of a constant flow past the glider by a fluid with constant density measuring only the instantaneous velocities at the various monitoring points. In the next steps, the addition of a dense net of monitoring points around the critical areas in the simulation (around the sensors, the wake of the glider) would be sensible so that the turbulent layer around the glider

body could be investigated precisely.
The idealised scenario of the glider configuration (angle of attack α, speed of the glider U) in our simulation stems from studies of i.e. Fer et al. (2014) and Palmer et al. (2015) as an average value of the dives completed by the gliders which is similar to the approach of Moat et al. (2016). With the variation of this configuration, we would expect the angle of attack to have a substantial impact on the flow properties around the sensors since its increase would enlarge the blockage effect of the glider geometry which would severely influence the undisturbed measurements at the sensor positions whereas a decrease could benefit the correct sampling of fluid properties. Increasing the flow speed would intensify the turbulent flow around the glider body and change the properties of the current laminar and turbulent flow regimes drastically, probably introduce vortex shedding at unwanted areas. The decrease of the flow speed would extent the laminar flow regime and might be helpful when lower ambient turbulence near the lower measurement threshold is targeted though the flight characteristics of the glider would change drastically with a profound loss of stability of the platform.
The measurement of the lift and drag forces with the Basilisk code is the most anticipated open question. The aforementioned sensitivity studies including different flow speeds in the simulation (and therefore different glider velocities when deploying the platform in the ocean) and varying angles of attack would provide lift and drag coefficients to be combined to the lift-drag ratio (L/D ratio) which could be compared with the experimental data of Lidtke et al. (2017). The forces of lift and especially the drag can be directly inserted into the model of Merckelbach et al. (2010, 2019) and provide an artificial, simulation-based set of parameters that could help to compare, identify and strengthen parameters in the quasi-static model of Merckelbach et al. (2010) and the new dynamic model (Merckelbach et al., 2019) for the steady glider flight.

Bibliography

J. Bardina, J. Ferziger, and W. Reynolds. Improved subgrid-scale models for large-eddy simulation. In *13th Fluid and PlasmaDynamics Conference*, page 1357, 1980.

N. Beaird, I. Fer, P. Rhines, and C. Eriksen. Dissipation of turbulent kinetic energy inferred from seagliders: An application to the eastern nordic seas overflows. *Journal of physical oceanography*, 42(12):2268–2282, 2012.

J. B. Bell, P. Colella, and H. M. Glaz. A second-order projection method for the incompressible navier-stokes equations. *Journal of Computational Physics*, 85(2):257–283, 1989.

M. J. Berger and J. Oliger. Adaptive mesh refinement for hyperbolic partial differential equations. *Journal of computational Physics*, 53(3):484–512, 1984.

P. Bhatta. *Nonlinear stability and control of gliding vehicles*. PhD thesis, Princeton University New Jersey, USA, 2006.

A. J. Chorin. Numerical solution of the navier-stokes equations. *Mathematics of computation*, 22(104):745–762, 1968.

B. Claus, R. Bachmayer, and L. Cooney. Analysis and development of a buoyancy-pitch based depth control algorithm for a hybrid underwater glider. In *2012 IEEE/OES Autonomous Underwater Vehicles (AUV)*, pages 1–6. IEEE, 2012.

J. M. Cusack, A. C. Naveira Garabato, D. A. Smeed, and J. B. Girton. Observation of a large lee wave in the drake passage. *Journal of Physical Oceanography*, 47(4):793–810, 2017.

C. C. Eriksen, T. J. Osse, R. D. Light, T. Wen, T. W. Lehman, P. L. Sabin, J. W. Ballard, and A. M. Chiodi. Seaglider: A long-range autonomous underwater vehicle for oceanographic research. *IEEE Journal of oceanic Engineering*, 26(4):424–436, 2001.

D. G. Evans, N. S. Lucas, V. Hemsley, E. Frajka-Williams, A. C. Naveira Garabato, A. Martin, S. C. Painter, M. E. Inall, and M. R. Palmer. Annual cycle of turbulent dissipation estimated from seagliders. *Geophysical Research Letters*, 45(19):10–560, 2018.

I. Fer, G. Voet, K. S. Seim, B. Rudels, and K. Latarius. Intense mixing of the faroe bank channel overflow. *Geophysical Research Letters*, 37(2), 2010.

I. Fer, A. K. Peterson, and J. E. Ullgren. Microstructure measurements from an underwater glider in the turbulent faroe bank channel overflow. *Journal of Atmospheric and Oceanic Technology*, 31(5):1128–1150, 2014.

A. C. N. Garabato, E. E. Frajka-Williams, C. P. Spingys, S. Legg, K. L. Polzin, A. Forryan, E. P. Abrahamsen, C. E. Buckingham, S. M. Griffies, S. D. McPhail, et al. Rapid mixing and exchange of deep-ocean waters in an abyssal boundary current. *Proceedings of the National Academy of Sciences*, 116(27):13233–13238, 2019.

J. G. Graver. *Underwater gliders: Dynamics, control and design*. PhD thesis, Princeton University New Jersey, USA, 2005.

J. Hinze. *Turbulence. An introduction to its mechanism and theory.* McGraw-Hill, 1959.

S. A. Jenkins, D. E. Humphreys, J. Sherman, J. Osse, C. Jones, N. Leonard, J. Graver, R. Bachmayer, T. Clem, P. Carroll, et al. Underwater glider system study. 2003.

J. Jeong and F. Hussain. On the identification of a vortex. *Journal of fluid mechanics*, 285: 69–94, 1995.

C. Jones, E. Creed, S. Glenn, J. Kerfoot, J. Kohut, C. Mudgal, and O. Schofield. Slocum gliders. a component of operational oceanography. In *Proc. 14th Int. Symp. on Unmanned Untethered Submersible Technology*, August 2005.

A. M. Khokhlov. Fully threaded tree algorithms for adaptive refinement fluid dynamics simulations. *Journal of Computational Physics*, 143(2):519–543, 1998.

P. Kundu, I. Cohen, and D. Dowling. *Fluid Mechanics*. Academic Press. Academic Press/Elsevier, 2012. ISBN 9780123821003.

E. Kunze. Internal-wave-driven mixing: Global geography and budgets. *Journal of Physical Oceanography*, 47(6):1325–1345, 2017.

J. Ledwell, E. Montgomery, K. Polzin, L. S. Laurent, R. Schmitt, and J. Toole. Evidence for enhanced mixing over rough topography in the abyssal ocean. *Nature*, 403(6766): 179–182, 2000.

J. R. Ledwell, L. C. St. Laurent, J. B. Girton, and J. M. Toole. Diapycnal mixing in the antarctic circumpolar current. *Journal of Physical Oceanography*, 41(1):241–246, 2011.

A. Lidtke, S. Lewis, T. Harvey, S. Turnock, and J. Downes. An experimental study into the effect of transitional flow on the performance of underwater glider wings. 2017.

R. G. Lueck, F. Wolk, and H. Yamazaki. Oceanic velocity microstructure measurements in the 20th century. *Journal of Oceanography*, 58(1):153–174, 2002.

J. MacKinnon and M. Gregg. Mixing on the late-summer new england shelf—solibores, shear, and stratification. *Journal of Physical Oceanography*, 33(7):1476–1492, 2003a.

L. Merckelbach, D. Smeed, and G. Griffiths. Vertical water velocities from underwater gliders. *Journal of Atmospheric and Oceanic Technology*, 27(3):547–563, 2010.

L. Merckelbach, A. Berger, G. Krahmann, M. Dengler, and J. R. Carpenter. A dynamic flight model for slocum gliders and implications for turbulence microstructure measurements. *Journal of Atmospheric and Oceanic Technology*, 36(2):281–296, 2019.

B. Moat, D. Smeed, C. Marcinko, S. Popinet, and S. Turnock. Flow distortion around underwater gliders and impacts on sensor measurements: a pilot study using large-eddy simulations. 2016.

J. N. Moum, D. R. Caldwell, and C. A. Paulson. Mixing in the equatorial surface layer and thermocline. *Journal of Geophysical Research: Oceans*, 94(C2):2005–2022, 1989.

W. Munk and C. Wunsch. Abyssal recipes ii: energetics of tidal and wind mixing. *Deep Sea Research Part I: Oceanographic Research Papers*, 45(12):1977–2010, 1998.

P. W. Nasmyth. *Oceanic turbulence*. PhD thesis, University of British Columbia, 1970.

M. Nikurashin and G. Vallis. A theory of deep stratification and overturning circulation in the ocean. *Journal of Physical Oceanography*, 41(3):485–502, 2011.

N. Oakey. Determination of the rate of dissipation of turbulent energy from simultaneous temperature and velocity shear microstructure measurements. *Journal of Physical Oceanography*, 12(3):256–271, 1982.

T. Osborn and W. Crawford. An airfoil probe for measuring turbulent velocity fluctuations in water. In *Air-Sea Interaction*, pages 369–386. Springer, 1980.

T. R. Osborn. Vertical profiling of velocity microstructure. *Journal of Physical Oceanography*, 4(1):109–115, 1974.

M. Palmer, G. Stephenson, M. Inall, C. Balfour, A. Düsterhus, and J. Green. Turbulence and mixing by internal waves in the celtic sea determined from ocean glider microstructure measurements. *Journal of Marine Systems*, 144:57–69, 2015.

M. R. Palmer, J. A. Polton, M. E. Inall, T. Rippeth, J. Green, J. Sharples, and J. Simpson. Variable behavior in pycnocline mixing over shelf seas. *Geophysical Research Letters*, 40(1):161–166, 2013.

R. Peyret and T. D. Taylor. *Computational methods for fluid flow*. Springer Science & Business Media, 2012.

K. Polzin, J. Toole, J. Ledwell, and R. Schmitt. Spatial variability of turbulent mixing in the abyssal ocean. *Science*, 276(5309):93–96, 1997.

S. B. Pope. *Turbulent Flows*. Cambridge University Press, 2000.

S. Popinet. Gerris: a tree-based adaptive solver for the incompressible euler equations in complex geometries. *Journal of Computational Physics*, 190(2):572–600, 2003.

S. Popinet. Gerris. http://gfs.sourceforge.net/wiki/index.php/, 2006–2010.

S. Popinet. An accurate adaptive solver for surface-tension-driven interfacial flows. *Journal of Computational Physics*, 228(16):5838–5866, 2009.

S. Popinet. Basilisk. http://basilisk.fr/, 2013–2019.

S. Popinet. A quadtree-adaptive multigrid solver for the serre–green–naghdi equations. *Journal of Computational Physics*, 302:336–358, 2015.

S. Popinet and G. Rickard. A tree-based solver for adaptive ocean modelling. *Ocean Modelling*, 16(3-4):224–249, 2007.

L. Rainville and P. Winsor. Mixing across the arctic ocean: Microstructure observations during the beringia 2005 expedition. *Geophysical Research Letters*, 35(8), 2008.

T. P. Rippeth, B. J. Lincoln, Y.-D. Lenn, J. M. Green, A. Sundfjord, and S. Bacon. Tide-mediated warming of arctic halocline by atlantic heat fluxes over rough topography. *Nature Geoscience*, 8(3):191–194, 2015.

B. Scheifele, S. Waterman, L. Merckelbach, and J. R. Carpenter. Measuring the dissipation rate of turbulent kinetic energy in strongly stratified, low-energy environments: A case study from the arctic ocean. *Journal of Geophysical Research: Oceans*, 123(8): 5459–5480, 2018.

L. K. Schultze, L. M. Merckelbach, and J. R. Carpenter. Turbulence and mixing in a shallow shelf sea from underwater gliders. *Journal of Geophysical Research: Oceans*, 122(11):9092–9109, 2017.

J. H. Simpson, W. R. Crawford, T. P. Rippeth, A. R. Campbell, and J. V. Cheok. The vertical structure of turbulent dissipation in shelf seas. *Journal of Physical Oceanography*, 26(8):1579–1590, 1996.

L. St. Laurent and C. Garrett. The role of internal tides in mixing the deep ocean. *Journal of Physical Oceanography*, 32(10):2882–2899, 2002.

L. St. Laurent and S. Merrifield. Measurements of near-surface turbulence and mixing from autonomous ocean gliders. *Oceanography*, 30(2):116–125, 2017.

L. St. Laurent, A. C. Naveira Garabato, J. R. Ledwell, A. M. Thurnherr, J. M. Toole, and A. J. Watson. Turbulence and diapycnal mixing in drake passage. *Journal of Physical Oceanography*, 42(12):2143–2152, 2012.

G. I. Taylor. Production and dissipation of vorticity in a turbulent fluid. *Proceedings of the Royal Society of London. Series A-Mathematical and Physical Sciences*, 164(916):15–23, 1938a.

G. I. Taylor. The spectrum of turbulence. *Proceedings of the Royal Society of London. Series A-Mathematical and Physical Sciences*, 164(919):476–490, 1938b.

S. A. Thorpe. *The turbulent ocean*. Cambridge University Press, 2005.

L. Umlauf and H. Burchard. Marine turbulence. http://www.io-warnemuende.de/lars-umlauf-teaching.html, May 2016. University lecture.

A. F. Waterhouse, J. A. MacKinnon, J. D. Nash, M. H. Alford, E. Kunze, H. L. Simmons, K. L. Polzin, L. C. St. Laurent, O. M. Sun, R. Pinkel, et al. Global patterns of diapycnal mixing from measurements of the turbulent dissipation rate. *Journal of Physical Oceanography*, 44(7):1854–1872, 2014.

C. Whalen, L. Talley, and J. MacKinnon. Spatial and temporal variability of global ocean mixing inferred from argo profiles. *Geophysical Research Letters*, 39(18), 2012.

C. B. Whalen, J. A. MacKinnon, L. D. Talley, and A. F. Waterhouse. Estimating the mean diapycnal mixing using a finescale strain parameterization. *Journal of Physical Oceanography*, 45(4):1174–1188, 2015.

C. D. Williams, R. Bachmayer, and B. deYoung. Progress in predicting the performance of ocean gliders from at-sea measurements. In *OCEANS 2008*, pages 1–8. IEEE, 2008.

F. Wolk, H. Yamazaki, L. Seuront, and R. G. Lueck. A new free-fall profiler for measuring biophysical microstructure. *Journal of Atmospheric and Oceanic Technology*, 19(5): 780–793, 2002.

F. Wolk, R. Lueck, and L. S. Laurent. Turbulence measurements from a glider. In *OCEANS 2009*, pages 1–6. IEEE, 2009.